Index Modulation-based Information Harvesting for Far-Field RF Power Transfer

M. Ertug Pihtili *Student Member, IEEE*, Mehmet C. Ilter *Senior Member, IEEE*, Ertugrul Basar *Fellow, IEEE*, Risto Wichman *Member, IEEE*, and Jyri Hämäläinen *Senior Member, IEEE*

Abstract—As wireless information transmission (WIT) progresses into its sixth generation (6G), a challenge arises in sustaining terminal operations with limited batteries for Internet-of-Things (IoT) platforms. To address this, wireless power transfer (WPT) emerges as a solution, empowering battery-less infrastructures and enabling nodes to harvest energy for sustainable operations. Thus, the eclectic integration of WPT with WIT mechanisms becomes crucial to mitigate the need for battery replacements while providing secure and reliable communication. A novel protocol that amalgamates WIT and WPT called *Information Harvesting (IH)* has recently been proposed to effectively handle challenges in wireless information and power transfer (WIPT) by employing index modulation (IM) techniques for data communication atop the existing far-field WPT mechanism. This paper presents a unified framework for IM-based IH mechanisms and evaluates their energy harvesting capability, bit error rate (BER), and ergodic secrecy rate (ESR) performance for diverse IM schemes. The findings indicate the significant potential of the IM-based IH mechanism in facilitating reliable data communication within existing far-field WPT systems while underscoring promising refinements in green and secure communication paradigms for next-generation IoT wireless networks.

Index Terms—Wireless power transfer, information harvesting, index modulation, energy harvesting, physical layer security.

I. INTRODUCTION

IN the 6G era, IoT platforms are required to support a massive number of devices and to tackle energy demands in addition to existing challenges in data transmission. In this respect, existing discussions in standardization frameworks are underway in ambient IoT scenarios [1], where IoT devices are able to harvest ambient energy from external sources. In this direction, zero-power communication technology [2] has been emerged as the next logical step in future networks and promises information transmission where its energy is harvested from surrounding radio frequency (RF) energy, thus reducing the need for replacing batteries [3]. To reach greater sustainability and environmentally friendly architectures, the

synergistic integration of various frameworks connecting energy harvesting with communication infrastructure appears to be an inevitable development in the near future.

The origin of WPT can be traced back to the seminal work of N. Tesla [4]. His idea was based on radiating the energy through a medium (i.e., air) with the help of antenna elements. Nowadays, the WPT has been extensively studied for RF signals [5], [6] and for visible light communications [7], which is an emerging 6G paradigm. The WPT can be broadly classified into two primary categories: near-field and far-field. Near-field WPT involves power transfer over short distances through magnetic fields using inductive coupling or electric fields between the energy harvester and the power transmitter, which is beyond the scope of this paper. On the other hand, far-field WPT leverages dedicated or ambient RF signals in the surrounding indoor or outdoor environment. Ambient WPT results from existing RF transmission and is coupled with backscattering techniques. Far-field WPT serves as an advantageous and sustainable power source for longer ranges [8]. In this aspect, the far-field WPT introduces viable solutions to tackle the battery depletion problem for wireless nodes/devices since RF energy harvesting allows wireless nodes to scavenge energy from the environment without tethering to electricity grids or requiring battery replacement, particularly in hazardous and inaccessible environments [9]. Thus, WPT is an emerging technology for various applications, including remote environmental monitoring, consumer electronics, biomedical implants, building/home automation, and logistics solutions [10].

In the far-field RF power transfer, one of the crucial focuses has been enhancing the RF-to-DC conversion efficiency of a rectenna, a combination of a rectifier and an antenna, serving as a key element in energy harvesting systems. Accordingly, developing efficient rectennas has been a longstanding focus in the literature [8]. These investigations have highlighted the significance of tailoring rectenna designs to match precise operating frequencies and input power levels, thus posing a significant challenge due to the inherent nonlinear characteristics in practical rectenna implementations [11].

Furthermore, the efficiency of RF energy harvesting also depends on the choice of a selected WPT waveform at the power transmitter. For instance, it has been demonstrated that deploying multitone waveforms enhances the efficiency of RF-to-DC conversion, thereby increasing the output DC power in flat-fading channels [12]. Aside from grid-based and lattice-based constellations used in conventional communication systems where low peak-to-average-power-ratio

M. Ertug Pihtili and E. Basar are with the Communications Research and Innovation Laboratory (CoreLab), Department of Electrical and Electronics Engineering, Koç University, Sariyer, Istanbul 34450, Turkey (e-mail: mpihtili22@ku.edu.tr; ebasar@ku.edu.tr).

Mehmet C. Ilter is with the Department of Electrical Engineering, Tampere University, Finland (e-mail:mehmet.ilter@tuni.fi).

Risto Wichman and Jyri Hämäläinen are with the Department of Information and Communications Engineering, Aalto University, Espoo, Finland (e-mail: risto.wichman@aalto.fi; jyri.hamalainen@aalto.fi).

(PAPR) is typically desired due to nonlinearity in power amplifiers, real Gaussian signals, flash signaling, and linear frequency-modulated signals are preferred in earlier far-field power harvesting mechanisms [8] at the cost of higher complexity and power consumption in the transmitter due to their higher PAPR. Interestingly, the effects of different modulation techniques, such as amplitude shift keying (ASK), quadrature amplitude modulation (QAM), phase-shift keying (PSK), and frequency shift keying (FSK) on battery charging time, are measured and theoretically analyzed in [13].

In RF energy harvesting systems, the concept of wireless-powered communication networks (WPCN) was initially introduced to reduce the operational burden associated with battery replacement/recharging [14]. In WPCN, network elements first harvest energy from signals transmitted by RF energy sources and then utilize this harvested energy for their upcoming communication periods. Over the last decade, the concept has evolved to include data communication within wireless power transfer, known as simultaneous wireless information and power transfer (SWIPT) for RF-based mechanisms [15]. More recently, a similar approach has been introduced for optical-based systems, termed simultaneous light information and power transfer (SLIPT) [16]. In these systems, the power and information components are primarily separated across different domains: the power domain (power splitting), time domain (time switching), and space domain (antenna splitting) [17]. This separation introduces a trade-off between information transfer and energy transfer, dependent on the design preferences for data and power transmission, as extensively investigated in existing literature [18]. SWIPT studies are also found in commercial RFID systems, particularly in communication from reader to RFID tags [19]. Furthermore, the SWIPT mechanism has been extended into multi-user scenarios, known as multi-user (MU)-SWIPT, where a multi-antenna transmitter simultaneously transmits wireless information and energy through spatial multiplexing to multiple single-antenna receivers [20].

It is essential to consider that most devices are simple nodes, i.e., RedCap devices [21], operating at a level of several kbps with limited computational capabilities. For these devices, the SWIPT mechanism might be impractical in real-world scenarios due to distinct device requirements, particularly in ensuring secure data transmission alongside a far-field WPT mechanism in simple devices. The findings in [22] illustrate a significant drop in power transfer efficiency over transmission distance in such systems when incorporating security enhancements for information transmission into the design. In response to this limitation, a distributed antenna-based SWIPT protocol was proposed in [23]. Additionally, in [24], information bits are embedded in the tone index of multi-sine waveforms as an alternative solution. Another approach involves creating a modulation signal within a vacant resource block of communication in an orthogonal frequency division multiplexing (OFDM) block, as introduced in [25].

Accordingly, there is a demand for further solutions to prevent the potential interception of confidential information by unintended users. While conventional encryption techniques prove valuable in many instances for securing data transmission,
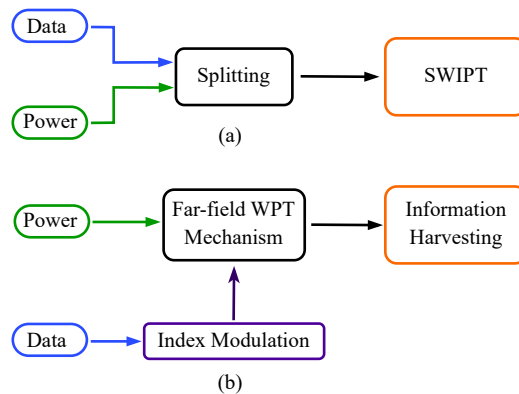

Fig. 1: The design aspects of (a) SWIPT and (b) Information Harvesting [26] mechanisms which show how data and power parts are integrated together.

there are specific use cases or protocols where implementing additional encryption is not feasible [27]. In this aspect, artificial noise (AN)-based physical layer security (PLS) techniques [28] turned into a powerful tool due to its ability to generate orthogonal noise through the channel state information between the transmitter and intended receiver. Considering its advantages against eavesdropping, the AN technique has been applied to multiple-input single-output (MISO) [29] and multiple-input multiple-output (MIMO) systems [30].

To address the efficiency losses in power transfer and to handle implementation concerns arising from differing sensitivities between the energy harvester and the data recipient, an alternative approach was proposed in [26]. This novel scheme, *Information Harvesting (IH)*, enables information transfer without disrupting the ongoing far-field wireless power transfer (WPT) mechanism between the power transmitter and the energy harvester. Fig. 1 compares the IH mechanism with SWIPT and depicts how the IH technique utilizes the existing far-field WPT mechanism to enable WIT through dedicated WPT waveforms. In the IH mechanism, WIT is achieved by injecting information into the indices of transmitter entities using index modulation (IM) schemes. This strategy contrasts with the SWIPT approach, which either employs different signaling schemes at the transmitter side or splits the received signal into various domains to deliver information and power to the intended receiving ends. Notably, the IH mechanism does not divide signals into different domains; instead, it distributes the total power among the active transmit antennas through the distinctive feature of IM schemes. This characteristic makes the IH mechanism adequate for extending the service area of the far-field WPT mechanism, overcoming the power transmission range challenge, which is a common limitation in SWIPT systems. Another superiority of the IM-based IH lies in its reduced pilot overhead since the MU-SWIPT system necessitates the channel state information (CSI) of both the information receiver (IR) and the energy harvester (EH) links. In contrast, the IH systems do not require CSI of the EH link, potentially leading to a reduced pilot overhead for channel estimation. The generalized space shift keying (GSSK)-based IH mechanism and its performance in terms of secrecy capacity and average harvested power was first investigated in [31]. Then,

[32] introduced a new IH mechanism that relies on quadrature spatial modulation (QSM).

In this paper, we introduce the IH architecture within a unified and comprehensive framework that encompasses a broader spectrum of IM techniques. We investigate the feasibility of these techniques while establishing unified performance criteria. In this aspect, our contributions can be summarized as follows:

- Currently, IH mechanisms are limited to space shift keying-based techniques and lack a broader perspective. This paper presents IM-based IH mechanisms comprehensively, addressing not only space shift keying-based techniques with no modulated symbol but also spatial modulation ones.
- Instead of focusing solely on specific performance metrics, our paper introduces a more comprehensive approach to performance evaluation. We analyze various IM-based IH mechanisms, taking into account their energy harvesting capability, bit error rate, and ergodic secrecy rate to provide valuable insights. Additionally, we present a unified framework to calculate the theoretical error performance of the proposed schemes. The simulated results are validated using analytical expressions for the bit error rate of the proposed IM-based IH mechanisms.
- The advantages of the IM-based IH mechanisms, particularly for far-field WPT range, have been demonstrated against existing SWIPT mechanisms, along with other practical advantages.

The remainder of this paper is organized as follows: In Section II, we present the general structure of IM-based IH model where the different implementations in the power transmitter based on the choice of IM technique, how the energy harvester and information receiver operate based on the chosen IM technique are introduced. The unified error performance analysis is given in Section III where the average bit error rate in the information receiver and the eavesdropper is derived, respectively. Section IV presents the ergodic capacity analysis in a similar manner, and the feasibility of the IM-based IH mechanism is investigated in Section V via a variety of simulation results along with the validation from the analysis. Section VI completes the paper with concluding remarks. For clarity, the abbreviations and notations in the text are listed in Table I.

II. IM-BASED INFORMATION HARVESTING MODEL

The block diagram of the IM-based IH mechanism is illustrated in Fig. 2, where the EH and the IR are located within the service area of the wireless power transmitter (WPTx) node, along with a potential malicious node, Eve. In the initial phase, assuming successful identification and synchronization between WPTx and an EH device, WPTx, equipped with a total of N_T transmit antennas, serves as the transmitting node responsible for sending multitone WPT waveforms across N distinct subbands into the service area for RF energy harvesting. When an IR device enters the service area, WPTx aims to transmit available information blocks to the IR. This is achieved by mapping the information blocks into vectors

TABLE I
ABBREVIATIONS AND NOTATIONS.

Abbreviation	Meaning
6G	Sixth generation
AN	Artificial noise
ASK	Amplitude shift keying
AWGN	Additive white Gaussian noise
BER	Bit error rate
CPEP	Conditional pairwise error probability
CSI	Channel state information
CSCG	Circularly symmetric complex Gaussian
CW	Continuous wave
DC	Direct current
EH	Energy harvester
EIRP	Effective Isotropic Radiated Power
ESR	Ergodic secrecy rate
FSK	Frequency shift keying
GSM	Generalized spatial modulation
GSSK	Generalized space shift keying
GQSM	Generalized quadrature spatial modulation
GQSSK	Generalized quadrature-based space shift keying
IH	Information harvesting/harvester
IR	Information receiver
IoT	Internet of Things
IM	Index modulation
ML	Maximum likelihood
MU-SWIPT	Multi-user simultaneous wireless information and power transfer
OFDM	Orthogonal frequency division multiplexing
PAPR	Peak to average power ratio
PDF	Probability density function
PLS	Physical layer security
QAM	Quadrature amplitude modulation
QSM	Quadrature spatial modulation
QSSK	Quadrature space shift keying
RF	Radio frequency
RFI	Request for information
RFID	Radio frequency identification
SLIPT	Simultaneous light-wave information and power transfer
SM	Spatial modulation
SSK	Space shift keying
SVD	Singular value decomposition
SWIPT	Simultaneous wireless information and power transfer
TS-SWIPT	Time switching simultaneous wireless information and power transfer
WIT	Wireless information transfer
WPCN	Wireless powered communication networks
WPT	Wireless power transfer
WPTx	Wireless power transmitter

Notation	Definition
x	Scalar values
$\mathbf{x}, \mathbf{X}$	Vectors/Matrices
$(\cdot)^T$	Transpose operation
$(\cdot)^H$	Hermitian transpose
$\lvert \cdot \rvert$	Absolute value
$\mathrm{rank}(\cdot)$	Rank of matrix
$\log_a(\cdot)$	Logarithm with base a
$\lVert \cdot \rVert$	Norm of vector/matrix
$\mathbb{E}[\cdot]$	Average operator
$\mathbb{E}_{\mathbf{x}}[\cdot]$	Statistical expectation with respect to random variable x
$P(\cdot)$	Probability of an event
$\lfloor \cdot \rfloor$	Floor operation
M	Modulation order
N	Number of subbands in WPT waveform
$p(\cdot)$	Probability density function
$\mathcal{Q}(x)$	Q-function
j	Imaginary unit, $\sqrt{-1}$
$\Re\{\cdot\}$	Real part
$\Im\{\cdot\}$	Imaginary part
$\mathcal{CN}(\mu, \sigma^2)$	CSCG random variable with a mean μ and a variance σ^2
$\mathbb{C}^{m \times n}$	A set of complex matrices of $m \times n$ dimensions
$\binom{n}{r}$	Binomial coefficient

corresponding to active transmit antennas, a process called *information seeding*. Meanwhile, the EH device, equipped with N_{EH} receive antennas, conducts recharging operations without any disruption. Notably, when the IR device enters the service area, there already exists a far-field WPT mechanism facilitated by a wireless link denoted as $\mathbf{G}_{\mathrm{EH}} \in \mathbb{C}^{N_{\mathrm{EH}} \times N_T \times N}$.

Subsequently, upon deployment, the IR device, which is equipped with N_{IR} receive antennas, initiates an information seeding cycle. This initiation is performed by transmitting a request-for-information (RFI) signal over a dedicated link represented by $\mathbf{H}_{\mathrm{IR}} \in \mathbb{C}^{N_{\mathrm{IR}} \times N_T \times N}$. The RFI signal may also
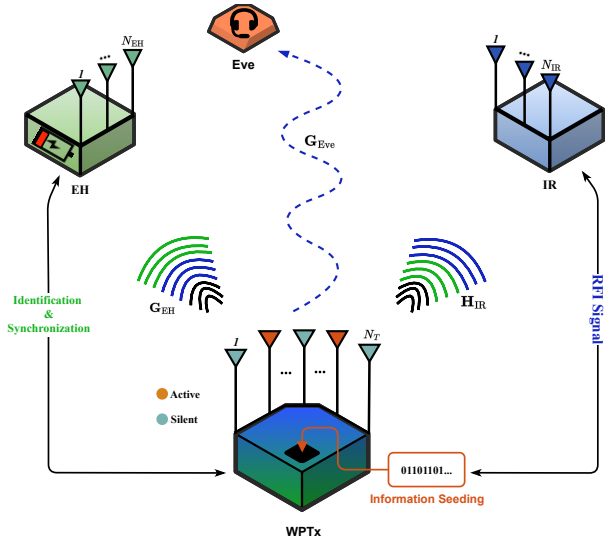
Fig. 2: The block diagram of the IM-based IH mechanism where the WPTx serves EH while sending its information to the IR by utilizing IM techniques with the existence of Eve in a service area.

include configuration parameters on the information seeding cycle, such as the frequency of changing the transmitting entity based on the required data rate within the IR and the necessity for additional PLS protocols [26]. Then, the information seeding process is initiated upon detecting the RFI signal at the WPTx. During this phase, the IR aims to capture variations resulting from the activation of various transmit antenna sets, which are determined by the information bits. This process is referred to as *information harvesting.* Importantly, it was demonstrated in [26] that activating more transmit antennas in WPTx during the power transfer period reduces the probability of detecting information seeding activity by devices located even in close proximity to the EH.

The channel entries are assumed to be independent and identically distributed (i.i.d.) according to $\mathcal{CN}(0,1)$. Note that the channels between the WPTx and other network elements in Fig. 2 are assumed to be stationary, so the time dependency of the channel coefficients is emitted from the channel coefficient and weight factors in the rest of the paper.

A. EH: Energy harvesting

During the period when the WPTx emits power transfer waveforms into a service area (regardless of the activation of information seeding cycle), the EH converts the received RF signal into DC output power thanks to its rectennas. Particularly, the EH consists of a receive antenna chain along with N_{EH} receive antennas, battery charging unit, and battery. Herein, the battery charging unit is configured to establish a link between the receive antenna chain and battery, wherein the manner in which power is transferred from the wireless power transceiver is controlled according to the parameters and/or state information assigned by the power management unit [32].

The EH device operates in two stages: firstly, the received RF power is converted into DC power using rectennas. Note that due to the nature of the wireless medium, there exists a fraction of time where the rectenna cannot perform harvesting since input RF power lies below certain RF power that is called

as *rectenna sensitivity* and after certain received signal power level at harvester, *rectenna saturation power*, the harvested energy stays constant as shown in [33]. After considering these practicalities as in [34], the output DC power for rectenna q can be formulated as a function of the received RF signal, which is,

$$v_{out,q} = \begin{cases} 0, & P_r^t \in [0, \Gamma_{in}] \\ \beta_2 P_r^t + \beta_4 P_r^{t2}, & P_r^t \in [\Gamma_{in}, \Gamma_{sat}] \\ \beta_2 \delta_{sat} + \beta_4 \delta_{sat}^2, & P_r^t \in [\Gamma_{in}, \Gamma_{sat}] \end{cases} \quad (1)$$

where P_r^t is the received input power during coherence period t, $P_r^t = \mathbb{E}[|y(t)|^2]$, Γ_{in} refers the harvester sensitivity, Γ_{sat} denotes the saturation level, β_2 and β_4 are the parameters of the nonlinear rectifier model. Then, the outputs of all rectennas are aggregated to obtain the cumulative harvested DC power at the combiner's output. This technique is referred to as DC combining, as discussed in [34]. Then, the total DC output power can be obtained from $\sum_{q=1}^{N_{\mathrm{EH}}} v_{out,q}^2 / R_L$ where R_L refers to the resistive load used to determine the output DC power.

In the nonlinear rectenna model, the calculation of the harvested DC power is not straightforward. For this purpose, [35] introduced a new technique where Taylor series expansion was applied into the nonlinear diode model. This approach provides insight into how the choices of the signal modulation or the input distributions affect the energy harvesting capability along with the configuration of the rectenna. Inspired from it, in this paper, the energy harvesting capability relates with a variable of z_{DC} which establishes a direct connection with (1) and reflects the harvested power when the signal operates within the bounds of the linear and saturation regions. Mathematically, z_{DC} is formulated as [35]

$$z_{\mathrm{DC}} = k_2 R_{\mathrm{ant}} \mathbb{E}[|y(t)|^2] + k_4 R_{\mathrm{ant}}^2 \mathbb{E}[|y(t)|^4], \quad (2)$$

where k_2 and k_4 represent the rectifier-dependent parameters, and R_{ant} denotes the antenna impedance. In a steady-state response, an ideal rectifier maintains a constant output voltage over time, and the level of this output voltage depends on the peaks of the input voltage. Therefore, z_{DC} can be improved as the number of subbands increases in the emitted waveform from the WPTx. This enhancement is particularly associated with the generation of larger peaks facilitated by multitone signals despite their average power being equivalent to that of continuous wave (CW) signals. The impact of multitone signals, which results in the generation of larger peaks, leads to a higher PAPR. Consequently, higher PAPR enhances the efficiency of the RF-to-DC conversion process in the nonlinear rectifier, contributing to an improved energy harvesting capability. In this respect, (2) demonstrates a positive correlation with PAPR, suggesting that modulation schemes or input distributions characterized by higher PAPR values offer advantages to the nonlinear rectenna model [36].

B. WPTx: Information seeding

In this subsection, we discuss the integration of different IM schemes into IH mechanism along with detailed description of the information seeding cycle. IM represents a unique approach to information transmission, achieved by selectively activating specific elements for conveying information. When information

seeding is initiated in WPTx alongside the specified IM scheme, the resulting set of waveforms emitted from the N_a activated WPTx antennas, obtained by combining an IM waveform at the WPTx, is as follows:

$$\mathbf{s} = \left[\frac{s_1(t)}{\sqrt{N_\mathrm{a}}}, 0, \ldots, 0, \frac{s_m(t)}{\sqrt{N_\mathrm{a}}}, 0, \ldots, 0, \frac{s_{N_\mathrm{a}}(t)}{\sqrt{N_\mathrm{a}}} \right], \quad (3)$$

at a given time instant t. Hereby, $s_m(t)$ is directly associated with the selection of the WPT waveform, $m \in \{1, \ldots, N_T\}$. For instance, when employing a multitone signal with N distinct subbands, the expression for $s_m(t)$ can be formulated as:

$$s_m(t) = \Re\left\{ \sum_{n=1}^{N} \omega_{n,m} e^{j2\pi f_n t} \right\}. \quad (4)$$

Hereby, N represents the number of subbands of multitone WPT signals, and f_n denotes the center frequency of the nth subband waveform. More specifically, $\omega_{n,m} = a_{n,m} e^{j\theta_{n,m}}$ where $a_{n,m}$ and $\theta_{n,m}$ are the nth subband amplitude and phase components of baseband WPT signal and these values are based on the chosen IM scheme. Subsequently, the received passband signal at the IR, without the additive white Gaussian noise (AWGN) term, can be expressed mathematically, as given in [35],

$$\mathbf{y}_\mathrm{IR}(t) = \Re\left\{ \sum_{n=1}^{N} \mathbf{G}_{\mathrm{EH},n} \mathbf{w}_n e^{j2\pi f_n t} \right\}, \quad (5)$$

where $\mathbf{G}_{\mathrm{EH},n}$ is the channel between WPTx and IR for nth subband and $\mathbf{w}_n = [\omega_{n,1} \ldots \omega_{n,N_T}]^T$, where the power of $\mathbf{w}_n$, denoted as λ_s^2/N (i.e., $\mathbb{E}[\mathbf{w}_n^H \mathbf{w}_n] = \lambda_s^2/N$), is arranged in accordance with the values of N and N_a.

1) GSSK/SSK-based IH: In the IH mechanism based on GSSK, the available information bits are exclusively mapped into a transmit antenna vector, determining the number of active transmit antennas denoted as N_a, with the constraint $N_\mathrm{a} \leq N_T$ [37], when $N_\mathrm{a} = 1$, it simplifies to the SSK-based IH mechanism. The number of information bits that can be mapped into the transmit antenna indices for GSSK modulation is given by:

$$\eta_\mathrm{GSSK} = \left\lfloor \log_2 \binom{N_T}{N_\mathrm{a}} \right\rfloor, \quad (6)$$

where $\lfloor \cdot \rfloor$ indicates floor operation. Under this assumption, the emitted WPT waveform does not contain any information components itself; instead, the antennas simply emit power transfer waveforms to the service area. From the EH perspective, there is no difference in the GSSK/SSK-based IH mechanism, as no signal modulation is employed, leading to $a_{n,m} = 1$ and $\theta_{n,m} = 0$. Note that $L = 2^\eta$ different active antenna combinations exist when N_a antennas are active out of total N_T transmit antennas, which is equal to the cardinality of the GSSK codebook.

2) GSM/SM-based IH: In the case of GSM-based IH, WPTx begins embedding information within the emitted symbol. This differs from the SSK-based techniques mentioned earlier, where only unmodulated WPT waveforms exist. Consequently, the number of transmitted information bits can be expressed as:

$$\eta_\mathrm{GSM} = \left\lfloor \log_2 \binom{N_T}{N_\mathrm{a}} \right\rfloor + \log_2 (M), \quad (7)$$

where M represents the modulation order of M-QAM constellation used in the WPTx. In the GSM-based IH

mechanism, $a_{n,m}$ and $\theta_{n,m}$ should be configured according to the employed M-QAM. For instance, in case of 4-QAM is utilized for GSM/SM-based IH mechanism, the $a_{n,m}$ and $\theta_{n,m}$ values can be set to $\{\sqrt{2}, 7\pi/4\}$ for a bit sequence of [01] in addition to the bits mapped into active antenna indices.

3) GQSSK/QSSK-based IH: Quadrature-based implementations require additional signal processing before transmission to the information seeding stage. The transmitted symbols are decomposed into in-phase and quadrature components, resulting in two transmit antenna vectors. The first transmit antenna vector corresponds to the real part of a wireless power symbol, while the second corresponds to the imaginary part [38]. Therefore the number of information bits increases to

$$\eta_\mathrm{GQSSK} = 2\eta_\mathrm{GSSK}. \quad (8)$$

Assuming $s_m(t)$ is a complex WPT signal, and its the real part, $\Re\{s_m(t)\}$, and its imaginary part, $\Im\{s_m(t)\}$, are transmitted separately through the different antennas over cosine and sine carriers respectively [38]. In the GQSSK/QSSK-based IH mechanism, the transmitted symbol is fixed and equal to $1 + j$. Consequently, the corresponding $a_{n,m}$ and $\theta_{n,m}$ values are $\{\sqrt{2}, \pi/4\}$.

4) GQSM/QSM-based IH: Similar to (7), now WPT signal carries the modulated symbol from M-ary constellation, and the real part modulates the in-phase part of the carrier, whereas the imaginary part modulates the quadrature component of the carrier signal. Then, the spectral efficiency of GQSM is given by

$$\eta_\mathrm{GQSM} = 2 \left\lfloor \log_2 \binom{N_T}{N_\mathrm{a}} \right\rfloor + \log_2 (M). \quad (9)$$

Without loss of generality, $a_{n,m}$ and $\theta_{n,m}$ values are drawn from M-QAM constellation points in this paper.

5) AN generation: AN is intentionally generated to safeguard against information leakage across the communication channel connecting WPTx and a potential eavesdropper (Eve) and is characterized by the channel matrix $\mathbf{G}_\mathrm{Eve} \in \mathbb{C}^{N_\mathrm{Eve} \times N_T \times N}$. Provided Eve possesses knowledge of the mapping rule utilized by the IM schemes, it could intercept the information transmission between WPTx and IR, thus being capable of conducting information harvesting. The primary objective of introducing this deliberately produced interference is to enhance the robustness of the PLS within the system to combat Eve, preventing it from decoding the information intended for IR.

For the AN generation, it is assumed that the IR has N_IR receive antennas such that $N_\mathrm{IR} < N_T$. Then, the singular value decomposition (SVD) can be implemented through each subband such that $\mathbf{H}_{\mathrm{IR},n} = \mathbf{U}_n \mathbf{\Lambda}_n \mathbf{V}_n^H$ where $\mathbf{H}_{\mathrm{IR},n}$ is a $N_\mathrm{IR} \times N_T$ channel matrix with $r = \mathrm{rank}(\mathbf{H}_{\mathrm{IR},n})$ and $\mathbf{V}_n = [\mathbf{v}_1^n \mathbf{v}_2^n \ldots \mathbf{v}_r^n \mathbf{v}_{r+1}^n \ldots \mathbf{v}_{N_T}^n]$ includes the nullspaces of $\mathbf{H}_{\mathrm{IR},n}$, which are $\mathbf{V}_{\perp,n} = [\mathbf{v}_{r+1}^n \ldots \mathbf{v}_{N_T}^n]$. Then, the AN waveform can be expressed as

$$\boldsymbol{\varepsilon}_n = \sum_{i=r+1}^{N_t} \delta_i \mathbf{v}_i^n u_i. \quad (10)$$

Herein, (10) is the jamming signal obtained from i.i.d. Gaussian distribution, $u_i \sim \mathcal{CN}(0, \lambda_u^2)$ along with $\sum_{i=r+1}^{N_t} \delta_i^2 = 1$. Since $\mathbf{H}_{\mathrm{IR},n} \cdot \mathbf{V}_{\perp,n} = 0$ holds, the generated

AN on top of the existing WPT waveform does not affect on the received signal in IR while it leads to additional jamming power in Eve side due to $\mathbf{G}_{\text{Eve},n} \cdot \mathbf{V}_{\perp,n} \neq 0$. Given that AN is generated based on the link between WPTx and IR, it also contributes to additional jamming power on the EH side; hence, $\mathbf{G}_{\text{EH},n} \cdot \mathbf{V}_{\perp,n} \neq 0$. Later, we will provide comprehensive insights into how this interference also plays a pivotal role in boosting the system's energy harvesting capability.

As a result, the AN-added received passband waveform at the EH can be expressed as

$$\mathbf{y}_{\text{EH}} = \Re \left\{ \sum_{n=1}^{N} \mathbf{G}_{\text{EH},n} \left[\mathbf{w}_n e^{j2\pi f_n t} + \boldsymbol{\varepsilon}_n e^{j2\pi f_1 t} \right] \right\}. \quad (11)$$

Herein, the AN waveform aligns with the frequency of the first subband, f_1, and its power defined as λ_u^2/N for nth subband (i.e., $\mathbb{E}[\boldsymbol{\varepsilon}_n^H \boldsymbol{\varepsilon}_n] = \lambda_u^2/N$). In (11), AWGN term is omitted, assuming that the antenna noise is negligible and not substantial enough to be harvested.

C. IR: Information harvesting

The primary objective of the IH mechanism is to extract information from the received WPT-IM waveform. To conduct this, the IR leverages both the mapping rule employed by the IM scheme and the CSI of the WPT-IR link. While energy can be directly harvested from the received RF signal, the IR must acquire the baseband version of the received signal for a specific subband n. Following downconversion and filtering processes, the resulting baseband signal at the IR is mathematically expressed as described in [39]

$$\mathbf{y}_{\text{IR},n} = \mathbf{H}_{\text{IR},n} \mathbf{x}_n + \mathbf{z}_{\text{IR},n}. \quad (12)$$

Here, $\mathbf{x}_n$ includes the WPT-IM waveform $\mathbf{w}_n$ along with the AN waveform $\boldsymbol{\varepsilon}_n$ such that $\mathbf{x}_n = \mathbf{w}_n + \boldsymbol{\varepsilon}_n$. In (12) $\mathbf{z}_{\text{IR},n} \in \mathbb{C}^{N_{\text{IR}} \times 1}$ denotes the noise vector, where its each element $z_{\text{IR},n} \sim \mathcal{CN}\left(0, \sigma_n^2\right)$ has a zero mean and a variance σ_n^2 for the nth subband. Consequently, the total received baseband signal at the IR can be represented as:

$$\mathbf{y}_{\text{IR}} = \sum_{n=1}^{N} \left[\mathbf{H}_{\text{IR},n} \mathbf{x}_n + \mathbf{z}_{\text{IR},n} \right]. \quad (13)$$

The IR employs a maximum likelihood (ML) detector to estimate transmitted bits from the WPT-IM waveform. Since various IM techniques can be employed for conveying information, the resulting ML representations vary based on the utilized IM scheme. Consequently, the optimum ML decoder representations are provided separately below.

1) GSSK/SSK-based IH: The GSSK technique involves selecting specific columns from each subband component of the channel matrix, $\mathbf{H}_{\text{IR},n}$ to transmit information bits. Accordingly, the product $\mathbf{H}_{\text{IR},n}\mathbf{x}_n$ yields the term $\mathbf{h}_{\text{IR},n}^l$, which corresponds to the channel coefficient set of the lth GSSK codebook out of L possible combinations in total. It is worth noting that in the case of SSK, only a single column of $\mathbf{H}_{\text{IR},n}$ is chosen. Therefore, for mechanisms based on GSSK/SSK, the ML detector is designed to estimate the transmit antenna indices when given the value of N_{a}. The ML procedure can be implemented as follows:

$$\hat{l}_{\text{IR}} = \underset{l \in \{1,\dots,L\}}{\arg\min} \sum_{n=1}^{N} \left\| \mathbf{y}_{\text{IR},n} - \mathbf{h}_{\text{IR},n}^l \right\|^2. \quad (14)$$

Here, $\hat{l}_{\text{IR}}$ represents the estimated antenna index.

2) GSM/SM-based IH: GSM/SM schemes differ from GSSK/SSK ones through the use of signal modulation, specifically M-QAM, to enhance spectral efficiency. In cases where the WPT waveform includes a modulated symbol, (14) can be rewritten as follows:

$$(\hat{l}_{\text{IR}}, \hat{\omega}) = \underset{l \in \{1,\dots,L\}, \omega \in \psi}{\arg\min} \sum_{n=1}^{N} \left\| \mathbf{y}_{\text{IR},n} - \mathbf{h}_{\text{IR},n}^l \omega \right\|^2. \quad (15)$$

Here, $\omega_{n,m}$ representation in (4) simplifies to a ω as IM schemes transmit identical symbols from N_{a} active antennas across all subbands. Thus, $\omega = a e^{j\theta}$ represents a symbol selected from an M-QAM constellation, ψ, and $\hat{\omega}$ is decoded transmitted symbol.

3) QSSK/GQSSK-based IH: Similar to the GSSK/SSK-based mechanism, the ML detector only needs to estimate the active antenna indices without performing symbol decoding. The distinction is that QSSK scheme activates two antennas at a time to convey quadrature components, whereas GQSSK might activate more than two antennas. Hence, the ML detector should jointly estimate in-phase and quadrature components, and it is given by

$$\left(\hat{l}_{\text{IR}}^{\Re}, \hat{l}_{\text{IR}}^{\Im} \right) = \underset{\substack{\mathbf{h}_{\text{IR}}^{\Re,l}, \mathbf{h}_{\text{IR}}^{\Im,l} \\ l \in \{1,\dots,L\}}}{\arg\min} \sum_{n=1}^{N} \left\| \mathbf{y}_{\text{IR},n} - \left[\mathbf{h}_{\text{IR},n}^{\Re,l} + j\mathbf{h}_{\text{IR},n}^{\Im,l} \right] \right\|^2. \quad (16)$$

Herein, $\mathbf{h}_{\text{IR}}^{\Re,l}$ and $\mathbf{h}_{\text{IR}}^{\Im,l}$ correspond to the lth potential codebook channel coefficient set of the WPTx-IR link out of L candidates for real part and imaginary part transmission, respectively. $\left(\hat{l}_{\text{IR}}^{\Re}, \hat{l}_{\text{IR}}^{\Im} \right)$ refers the estimated indices of active transmit antennas at the IR. For a toy example, $\left(\hat{l}_{\text{IR}}^{\Re}, \hat{l}_{\text{IR}}^{\Im} \right) = ([110], [011])$ implies the 1st and 2nd transmit antennas are active for the real part and 2nd and 3rd for the imaginary part, respectively.

4) GQSM/QSM-based IH: GQSM/QSM augments QSSK/GQSSK techniques by incorporating M-QAM constellation symbols to transmit quadrature components, separately containing the in-phase and quadrature part of the M-QAM symbol. If the WPT-IM waveform contains a modulated symbol, (16) can be rewritten as follows:

$$\left(\hat{l}_{\text{IR}}^{\Re}, \hat{l}_{\text{IR}}^{\Im}, \hat{\omega} \right) =$$
$$\underset{\substack{\mathbf{h}_{\text{IR},n}^{\Re,l}, \mathbf{h}_{\text{IR},n}^{\Im,l} \\ l \in \{1,\dots,L\}, \omega \in \psi}}{\arg\min} \sum_{n=1}^{N} \left\| \mathbf{y}_{\text{IR},n} - \left[\mathbf{h}_{\text{IR},n}^{\Re,l} \Re\{\omega\} + j\mathbf{h}_{\text{IR},n}^{\Im,l} \Im\{\omega\} \right] \right\|^2, \quad (17)$$

where $\hat{\omega}$ is a decoded transmitted symbol whose real and imaginary parts are carried by different active transmit antennas.

III. ERROR PERFORMANCE ANALYSIS

In this section, average bit error rates (ABER) at the IR and the Eve are calculated, respectively.

A. ABER of Information receiver

The conditional pairwise error probability (CPEP) of deciding on a baseband IM codebook $\boldsymbol{x}_k$ in the case of that

$\boldsymbol{x}_j$ transmitted under ML detection can be calculated by [38]

$$P(\boldsymbol{x}_j \to \boldsymbol{x}_k \mid \mathbf{H}_{\text{IR}}) =$$

$$P\left(\left\|\sum_{n=1}^{N} \mathbf{z}_{\text{IR},n}\right\|^2 > \left\|\sum_{n=1}^{N} \mathbf{H}_{\text{IR},n}\left(\mathbf{w}_n^j - \mathbf{w}_n^k\right) + \mathbf{z}_{\text{IR},n}\right\|^2 \middle| \mathbf{H}_{\text{IR}}\right) =$$

$$P\left(2\Re\left\{\sum_{n=1}^{N} \mathbf{z}_{\text{IR},n}^H\left(\mathbf{h}_{\text{IR},n}^j \omega_j - \mathbf{h}_{\text{IR},n}^k \omega_k\right)\right\} > \left\|\sum_{n=1}^{N}\left(\mathbf{h}_{\text{IR},n}^j \omega_j - \mathbf{h}_{\text{IR},n}^k \omega_k\right)\right\|^2 \middle| \mathbf{H}_{\text{IR}}\right)$$

$$= \mathcal{Q}\left(\sqrt{\sum_{i=1}^{N_{\text{IR}}} \frac{\sum_{n=1}^{N} |\Phi_{\text{IR},i}^{(n)}|^2}{2N\sigma^2}}\right) = \mathcal{Q}\left(\sqrt{\gamma_{\text{IR}}}\right). \tag{18}$$

Herein, $\Phi_{\text{IR},i}^{(n)}$ is defined as $\Phi_{\text{IR},i}^{(n)} = (h_{\text{IR},n,i}^{\Re,j}\omega_j^{\Re} - h_{\text{IR},n,i}^{\Re,k}\omega_k^{\Re}) + (h_{\text{IR},n,i}^{\Im,j}\omega_j^{\Im} - h_{\text{IR},n,i}^{\Im,k}\omega_k^{\Im})$. Note that (18) introduces a generalized CPEP expression, and it can be utilized for calculating the different types of the IM schemes, ranging from the ones that do not employ modulated symbols to the ones that also carry a set of modulated symbols. The corresponding expressions for $\boldsymbol{\Phi}_{\text{IR}}^{(n)}$ are presented in Table II.

1) IM schemes with one active Tx per index: To begin with, $\Phi_{\text{IR}}^{(n)}$ can be simplified for the SSK and GSSK schemes by considering $\omega_j^{\Re} = \omega_k^{\Re} = \omega_j^{\Im} = \omega_k^{\Im} = 1$, and for the QSSK and GQSSK schemes by considering $\omega_j^{\Re} = \omega_k^{\Re} = 1$ and $\omega_j^{\Im} = \omega_k^{\Im} = j$. This simplification is applicable to the IM schemes that do not employ signal modulation, namely SSK, GSSK, QSSK, and GQSSK.

2) IM schemes with one multiple Tx per index: In the case of generalized IM schemes, that are GSSK, GSM, GQSSK, and GQSM, that simultaneously activate multiple antennas instead of single one, the corresponding effective channel columns $\mathbf{h}_{\text{IR},n,i}^{j_{\text{eff}}}$ and $\mathbf{h}_{\text{IR},n,i}^{k_{\text{eff}}}$ are considered in the ABER calculation since it represents the summation of the columns corresponding to active transmit antennas in the channel matrix of $\mathbf{H}_{\text{IR}}$.

3) IM schemes with modulated symbol: If there is signal modulation involved, ω is drawn from M-QAM contellation points on top of antenna indices for SM, GSM, QSM, and GQSM schemes.

Then, (18) implies that γ_{IR} follows a central chi-square distribution with $2N_{\text{IR}}$ degrees of freedom and it can be written as $\gamma_{\text{IR}} = \Sigma_{r=1}^{N_{\text{IR}}} |\nu_r^{\text{IR}}|^2$. Herein, $\nu_r^{\text{IR}} = \Sigma_{n=1}^{N}(h_{\text{IR},n,r}^j \omega_j - h_{\text{IR},n,r}^k \omega_k)/\sqrt{2\sigma_n^2}$ represents the rth element of $\boldsymbol{\Phi}_{\text{IR}}^{(n)}$, which has a row length of N_{IR}.

Remark 1: Assuming that ω_j and ω_k are drawn from real constellation points and equal to 1, such that γ_{IR} reduces to $\gamma_{\text{IR}} = \Sigma_{r=1}^{N_{\text{IR}}}\left(\Sigma_{n=1}^{N}|h_{\text{IR},n,r}^j - h_{\text{IR},n,r}^k|^2/2\sigma_n^2\right)$. Since there is a constraint on transmit power $\Sigma_{n=1}^{N}\|\mathbf{w}_n\|^2 \leq P_T$, and λ_s^2

TABLE II: CORRESPONDING $\Phi_{\text{IR}}^{(n)}$ EXPRESSIONS FOR THE USED IM SCHEMES.

IM Scheme	$\Phi_{\text{IR}}^{(n)}$
SSK	$(\mathbf{h}_{\text{IR},n,i}^j - \mathbf{h}_{\text{IR},n,i}^k)$
QSSK	$(\mathbf{h}_{\text{IR},n,i}^{\Re,j} - \mathbf{h}_{\text{IR},n,i}^{\Re,k}) + j(\mathbf{h}_{\text{IR},n,i}^{\Im,j} - \mathbf{h}_{\text{IR},n,i}^{\Im,k})$
SM	$(\mathbf{h}_{\text{IR},n,i}^j \omega_j - \mathbf{h}_{\text{IR},n,i}^k \omega_k)$
QSM	$(\mathbf{h}_{\text{IR},n,i}^{\Re,j}\omega_j^{\Re} - \mathbf{h}_{\text{IR},n,i}^{\Re,k}\omega_k^{\Re}) + (\mathbf{h}_{\text{IR},n,i}^{\Im,j}\omega_j^{\Im} - \mathbf{h}_{\text{IR},n,i}^{\Im,k}\omega_k^{\Im})$
GSSK	$(\mathbf{h}_{\text{IR},n,i}^{j_{\text{eff}}} - \mathbf{h}_{\text{IR},n,i}^{k_{\text{eff}}})$
GQSSK	$(\mathbf{h}_{\text{IR},n,i}^{\Re,j_{\text{eff}}} - \mathbf{h}_{\text{IR},n,i}^{\Re,k_{\text{eff}}}) + j(\mathbf{h}_{\text{IR},n,i}^{\Im,j_{\text{eff}}} - \mathbf{h}_{\text{IR},n,i}^{\Im,k_{\text{eff}}})$
GSM	$(\mathbf{h}_{\text{IR},n,i}^{j_{\text{eff}}}\omega_j - \mathbf{h}_{\text{IR},n,i}^{k_{\text{eff}}}\omega_k)$
GQSM	$(\mathbf{h}_{\text{IR},n,i}^{\Re,j_{\text{eff}}}\omega_j^{\Re} - \mathbf{h}_{\text{IR},n,i}^{\Re,k_{\text{eff}}}\omega_k^{\Re}) + (\mathbf{h}_{\text{IR},n,i}^{\Im,j_{\text{eff}}}\omega_j^{\Im} - \mathbf{h}_{\text{IR},n,i}^{\Im,k_{\text{eff}}}\omega_k^{\Im})$

is distributed equally among the elements of $\mathbf{w}_n$, introducing more subbands has no effect on $|h_{\text{IR},n,r}^j - h_{\text{IR},n,r}^k|$. Nonetheless, increasing the number of subbands, N, scales the numerator term of γ_{IR} by $1/(2\Sigma_{n=1}^{N}\sigma_n^2)$. Hence, an increase in N negatively affects the performance of the IH mechanism.

The average PEP, $P(\boldsymbol{x}_j \to \boldsymbol{x}_k)$, is written as follows [40]:

$$P(\boldsymbol{x}_j \to \boldsymbol{x}_k) = \xi^{N_{\text{IR}}} \sum_{i=0}^{N_{\text{IR}}-1} \binom{N_{\text{IR}} - 1 + i}{i} [1 - \xi]^i \tag{19}$$

where $\xi = (1 - \sqrt{(\bar{\nu}/2)/(1 + \bar{\nu}/2)})/2$ and $\bar{\nu}$ represents the mean value of ν_r^{IR} as detailed in [38]. After applying (19) and utilizing the well-known union bound expression, the generalized ABER expression for the IM-based IH mechanism can be calculated as follows:

$$\text{ABER} = \frac{1}{\eta}\frac{1}{L}\sum_{j=1}^{L}\sum_{k \neq j=1}^{L} \epsilon(j,k)\, P(\boldsymbol{x}_j \to \boldsymbol{x}_k) \tag{20}$$

where $\epsilon(j,k)$ is the number of erroneous bits when a codeword $\boldsymbol{x}_k$ is decoded at the IR when $\boldsymbol{x}_j$ is transmitted at the WPTx.

B. ABER of Eavesdropper

In this subsection, the ABER expression at the Eve is investigated, and the results herein can be utilized for evaluating a potential case where the EH acts in a malicious role such that EH tries to intercept information transmission intended for an information receiver for a given service area. To begin with, similar to (18), the conditional PEP expression for Eve can be expressed as follows:

$$P(\boldsymbol{x}_j \to \boldsymbol{x}_k \mid \mathbf{G}_{\text{Eve}}) =$$

$$P\left(\left\|\sum_{n=1}^{N} \Psi_n\left(\mathbf{G}_{\text{Eve},n}\boldsymbol{\varepsilon}_n + \mathbf{z}_{\text{Eve},n}\right)\right\|^2 \right.$$

$$\left. > \left\|\sum_{n=1}^{N} \Psi_n\left[\mathbf{G}_{\text{Eve},n}\left(\mathbf{w}_n^j - \mathbf{w}_n^k\right) + \mathbf{G}_{\text{Eve},n}\boldsymbol{\varepsilon}_n + \mathbf{z}_{\text{Eve},n}\right]\right\|^2 \middle| \mathbf{G}_{\text{Eve}}\right) \tag{21}$$

The expression $\hat{\Phi}_{\text{Eve},i}^{(n)}$ is defined as $\hat{\Phi}_{\text{Eve},i}^{(n)} = (g_{\text{Eve},n,i}^{\Re,j}\omega_j^{\Re} - g_{\text{Eve},n,i}^{\Re,k}\omega_k^{\Re}) + (g_{\text{Eve},n,i}^{\Im,j}\omega_j^{\Im} - g_{\text{Eve},n,i}^{\Im,k}\omega_k^{\Im})$, and it is obtained after applying the whitening transformation. The term $\Psi_n = \sigma_n \mathbf{C}_\epsilon^{-1/2}$ represents the whitening transformation matrix, where $\mathbf{C}_\epsilon$ is the covariance matrix of the interference plus noise term at Eve, given by:

$$\mathbf{C}_\epsilon = \frac{\lambda_u^2}{N(N_T - r)}\mathbf{G}_{\text{Eve},n}\left(\sum_{i=r+1}^{N_T} \mathbf{v}_i^n \mathbf{v}_i^{n^H}\right)\mathbf{G}_{\text{Eve},n}^H + \sigma_n^2 \mathbf{I}. \tag{22}$$

Note that the power of Ψ_n needs to be arranged based on the total number of available subbands and after multiplying Ψ_n with given WPT-IM waveforms, (21) reduces to

$$P(\boldsymbol{x}_j \to \boldsymbol{x}_k \mid \mathbf{G}_{\text{Eve}}) = \mathcal{Q}\left(\sqrt{\sum_{i=1}^{N_{\text{Eve}}} \frac{\sum_{n=1}^{N}|\hat{\Phi}_{\text{Eve},i}^{(n)}|^2}{2(N\sigma^2 + \lambda_u^2)}}\right) = \mathcal{Q}\left(\sqrt{\gamma_{\text{Eve}}}\right). \tag{23}$$

Herein, $\gamma_{\text{Eve}} = \Sigma_{r=1}^{N_{\text{Eve}}}|\nu_r^{\text{Eve}}|^2$ shows the similar characteristics with γ_{IR} given in (18) and the parameter $\nu_r^{\text{Eve}} = \Sigma_{n=1}^{N}(g_{\text{Eve},n,r}^j \omega_j - g_{\text{Eve},n,r}^k \omega_k)/\sqrt{2\sigma_n^2 + 2\lambda_u^2}$ signifies the r-th element of the vector $\hat{\boldsymbol{\Phi}}_{\text{Eve}}^{(n)}$, which has a row length of N_{Eve}. In this regard, the selection of $\hat{\boldsymbol{\Phi}}_{\text{Eve}}^{(n)}$ should be aligned with the selected IM schemes for information harvesting, as in the selection of $\boldsymbol{\Phi}_{\text{IR}}^{(n)}$. Then, the calculation of the ABER at the Eve can be obtained after substituting (23) into (20).

Remark 2: Obeying the same constraint on P_T and following the assumption that ω_j and ω_k are drawn from real constellation points and equal to 1, γ_{Eve} reduces to $\gamma_{\text{Eve}} = \Sigma_{r=1}^{N_{\text{Eve}}} \left(\Sigma_{n=1}^{N} |g_{\text{Eve},n,r}^j - g_{\text{Eve},n,r}^k|^2 / \left(2\sigma_n^2 + 2\lambda_u^2 \right) \right)$. Therefore, the numerator term of γ_{Eve} is scaled by a factor of $1/\left(2\Sigma_{n=1}^{N}\sigma_n^2 + 2\lambda_u^2 \right)$, which means that increasing N will lower the performance of Eve. As the SNR increases, and given that P_T is constant, λ_u^2 will progressively dominate over σ_n^2, especially when $\lambda_u^2 \gg \Sigma_{n=1}^{N}\sigma_n^2$, resulting in performance saturation, leading to identical performance across all values of N.

IV. ERGODIC SECRECY RATE ANALYSIS

In this section, we provide a generalized analytical framework of the ergodic secrecy rate for the proposed IM-based information harvesting schemes.

To do so, the GQSSK-based IH mechanism was considered. In this respect, each transmit antenna set for the real and the imaginary parts is selected with the same probability, $1/L$. Then, the received signal at the IR through N band, $\mathbf{y}_{\text{IR}}$, obeys the following distribution [41]

$$p\left(\mathbf{y}_{\text{IR}}\right) = \frac{1}{L^2} \sum_{j=1}^{L} \sum_{k=1}^{L} \frac{1}{\pi\sigma_n^2} e^{-\frac{\|\mathbf{r}_{\text{IR}}\|^2}{\sigma_n^2}}. \tag{24}$$

Here, $\mathbf{r}_{\text{IR}} = \mathbf{y}_{\text{IR}} - \mathbf{h}_{\text{IR}}^{\Re,j}\Re\{\omega\} - j\mathbf{h}_{\text{IR}}^{\Im,k}\Im\{\omega\}$ for a transmitted WPT signal, ω. Then, the mutual information, $\mathcal{I}_{\text{IR}}\left(\mathbf{r}_{\text{IR}}\right)$, can be expressed in (25), which is a special case of [Eq. (14), [41]]. Therein, $\mathbf{d}_{l_1,l_2}^{r_1,r_2}$ is defined as:

$$\mathbf{d}_{l_1,l_2}^{r_1,r_2} = \mathbf{h}_{\text{IR}}^{\Re,l_2\text{eff}}\Re\{\omega\} + j\mathbf{h}_{\text{IR}}^{\Im,l_1\text{eff}}\Im\{\omega\} - \mathbf{h}_{\text{IR}}^{\Re,r_1\text{eff}}\Re\{\omega\} - j\mathbf{h}_{\text{IR}}^{\Im,r_2\text{eff}}\Im\{\omega\} \tag{27}$$

where $\mathbf{h}_{\text{IR}}^{\text{eff}}$ is the effective channel after incorporating only active transmit antenna set at the IR such that $\mathbf{h}_{\text{IR}}^{i\text{eff}} = \mathbf{h}_{\text{Eve}}^{i,1} + \cdots + \mathbf{h}_{\text{Eve}}^{i,N_a}$ [42]. Similar to (24), the received signal at the Eve obeys the following distribution [41]

$$p\left(\mathbf{y}_{\text{Eve}}\right) = \frac{1}{L^2} \sum_{j=1}^{L} \sum_{k=1}^{L} \frac{1}{\pi\sigma_n^2} e^{-\frac{\|\mathbf{r}_{\text{Eve}}\|^2}{\sigma_n^2}}. \tag{28}$$

Therein, $\mathbf{r}_{\text{Eve}} = \mathbf{y}_{\text{IR}} - \mathbf{g}_{\text{Eve}}^{\Re,j}\Re\{\omega\} - j\mathbf{g}_{\text{Eve}}^{\Im,k}\Im\{\omega\}$. After accounting for the existence of the AN at the Eve side, the mutual information at Eve, $\mathcal{I}_{\text{Eve}}\left(\mathbf{r}_{\text{Eve}}\right)$, is given in (26), which is a special case of [Eq. (15), [41]]. Here, $\mathbf{z}_{\text{Eve}}$ is the Gaussian noise at the Eve and $\boldsymbol{\delta}_{l_1,l_2}^{r_1,r_2}$ can be expressed as:

$$\boldsymbol{\delta}_{l_1,l_2}^{r_1,r_2} = \mathbf{C}_\epsilon^{-\frac{1}{2}} \left(\mathbf{g}_{\text{Eve}}^{\Re,l_2\text{eff}}\Re\{\omega\} + j\mathbf{g}_{\text{Eve}}^{\Im,l_1\text{eff}}\Im\{\omega\} \right) - \mathbf{C}_\epsilon^{-\frac{1}{2}} \left(\mathbf{g}_{\text{Eve}}^{\Re,r_1\text{eff}}\Re\{\omega\} - j\mathbf{g}_{\text{Eve}}^{\Im,r_2\text{eff}}\Im\{\omega\} \right), \tag{29}$$

where $\mathbf{g}_{\text{Eve}}^{i\text{eff}}$ is the effective channel.

Note that the channel between the WPTx and the IR relies on GQSSK-based modulated antenna indices, so the capacity analysis deducts into a capacity analysis for the discrete-input continuous-output memoryless channel (DCMC) [43], and it might be not straightforward to obtain the closed-form analysis in most cases. In this respect, the secrecy rate of IR can be expressed as [42]

$$\mathcal{R}_{\text{IR}} = \max\{0, \ \mathcal{I}_{\text{IR}}\left(\mathbf{y}_{\text{IR}}\right) - \mathcal{I}_{\text{Eve}}\left(\mathbf{y}_{\text{Eve}}\right)\}, \tag{30}$$

Note that positive secrecy from (30) implies communication opportunity on top of the existing WPT mechanism, even if some information can be leaked to Eve in the service area.

For the other IM schemes given in Section II.B, the ergodic secrecy rates can be obtained from (30) after modifying (25) and (26) where L^2 results in exploiting two different active antenna sets for real and imaginary parts of the emitted waveforms where L is the number of available antenna combinations for each part. For instance, in the case of GQSM/QSM-based IH, the summation limits should be replaced with $L \to LM$ where M is the modulation order and ω seen in (27) becomes a variable of the summation indices rather than constant waveform such that ω_{l_1}.

For GQSSK/SSK schemes, the secrecy calculation requires one effective channel definition without dividing real and imaginary parts so the definition of $\mathbf{r}_{\text{IR}}$ in (24) is reformulated as $\mathbf{r}_{\text{IR,n}} = \mathbf{y}_{\text{IR,n}} - \mathbf{h}_j^n\omega$ [42] which results in

$$\mathcal{I}_{\text{IR}}\left(\mathbf{y}_{\text{IR}}\right) = \log_2\left(L\right)$$
$$- \frac{1}{L} \sum_{l_1=1}^{L} \mathbb{E}_{\mathbf{z}_{\text{IR}}} \left[\log_2 \left(\sum_{l_2=1}^{L} e^{-\frac{\left\|\mathbf{d}_{l_1}^{l_2} + \mathbf{z}_{\text{IR}}\right\|^2 - \|\mathbf{z}_{\text{IR,n}}\|^2}{\sigma_n^2}} \right) \right]. \tag{31}$$

A similar approach is functional when considering the scenario involving Eve, where its mutual information can be expressed as follows:

$$\mathcal{I}_{\text{Eve}}\left(\mathbf{y}_{\text{Eve}}\right) = \log_2\left(L\right)$$
$$- \frac{1}{L} \sum_{l_1=1}^{L} \mathbb{E}_{\mathbf{z}_{\text{Eve}}} \left[\log_2 \left(\sum_{l_2=1}^{L} e^{-\frac{\left\|\boldsymbol{\varrho}_{l_1}^{l_2} + \mathbf{z}_{\text{Eve}}\right\|^2 - \|\mathbf{z}_{\text{Eve}}\|^2}{\sigma_n^2}} \right) \right]. \tag{32}$$

Herein, $\mathbf{d}_{l_1}^{l_2}$ and $\boldsymbol{\varrho}_{l_1}^{l_2}$ correspond to the channel distances between m_1th and m_2th antenna index combinations at the IR and the Eve for the nth subband, where N_a antennas out of N_T are active such that $\mathbf{d}_{l_1}^{l_2} = \mathbf{h}_{l_1,\text{eff}} - \mathbf{h}_{l_2,\text{eff}}$ and $\boldsymbol{\varrho}_{l_1}^{l_2} = \mathbf{g}_{l_1,\text{eff}} - \mathbf{g}_{l_2,\text{eff}}$, respectively. For GSM/SM-based IH, the summation limits should be replaced with $L \to LM$ where M is the modulation order, the calculation of $\mathbf{d}_{l_1}^{l_2}$ takes into account ω as in [42].

V. NUMERICAL RESULTS

In this section, we explore the feasibility of IM-based IH schemes in terms of their energy harvesting capability, bit error rate (BER), and ergodic secrecy rate (ESR) performances under various system setups where multitone signals are utilized for far-field WPT transmissions. The comparison involves diverse IM schemes, including GSSK with $N_T = 24$, GSM with $N_T = 8$, and 16-QAM, SM with $N_T = 16$, and 16-QAM, as well as SM with $N_T = 64$ and 4-QAM. Also, QSM with $N_T = 8$ and 4-QAM, QSSK with $N_T = 16$, GQSM with $N_T = 5$ and 4-QAM, and GQSSK with $N_T = 7$ and 4-QAM. Note that all IM schemes share a common spectral efficiency of $\eta = 8$, and in all scenarios, N_a and N_{EH} are set to 2 and 4, respectively. The channels between WPTx and EH, as well as between WPTx and IR, are assumed to be Rayleigh fading

TABLE III: SIMULATION PARAMETERS USED IN IM-based IH.

Parameter	Value	Reference
k_2, k_4	0.0034, 0.3829	[36]
d	$[1, 6]$	-
Path-loss model	$35.3 + 37.6\log_{10}(d)$	[31]
R_{ant}	50 Ω	[36]
P_T	36 dBm	-
N	$\{1, 3, 5\}$	-

$$\mathcal{I}_{\text{IR}}\left(\mathbf{y}_{\text{IR}}\right) = \log_2\left(L^2\right) - \frac{1}{L^2}\sum_{l_1=1}^{L}\sum_{l_2=1}^{L}\mathbb{E}_{\mathbf{z}_{\text{IR}}}\left[\log_2\left(\sum_{r_1=1}^{L}\sum_{r_2=1}^{L}e^{-\frac{\left\|\mathbf{d}_{l_1,l_2}^{r_1,r_2}+\mathbf{z}_{\text{IR}}\right\|^2-\|\mathbf{z}_{\text{IR}}\|^2}{\sigma^2}}\right)\right]. \tag{25}$$

$$\mathcal{I}_{\text{Eve}}\left(\mathbf{y}_{\text{Eve}}\right) = \log_2\left(L^2\right) - \frac{1}{L^2}\sum_{l_1=1}^{L}\sum_{l_2=1}^{L}\mathbb{E}_{\mathbf{z}_{\text{Eve}}}\left[\log_2\left(\sum_{r_1=1}^{L}\sum_{r_2=1}^{L}e^{-\frac{\left\|\boldsymbol{\delta}_{l_1,l_2}^{r_1,r_2}+\mathbf{z}_{\text{Eve}}\right\|^2-\|\mathbf{z}_{\text{Eve}}\|^2}{\sigma^2}}\right)\right]. \tag{26}$$

channels. Considering that the EH's energy scavenging ability is directly impacted by the distance between the transmitter and receiver [44], we utilize the following path loss model: $35.3 + 37.6\log_{10}(d)$, where d represents the distance between WPTx and EH. The EH is assumed to consist of N_{EH} pairs of receive antennas and rectennas, with perfect matching and an ideal low-pass filter assumed in rectennas.

In order to limit the maximum effective isotropic radiated power (EIRP) as specified in FCC Title 47, Part 15 regulations [45], the total transmit power is considered as $P_T = 36$ dBm at the WPTx. The total transmit power, P_T, is divided into AN and IM parts based on the power allocation factor ρ ($0 \le \rho \le 1$). Mainly, $\lambda_u^2 = \rho P_T$ represents the transmit power of the AN waveform, and $\lambda_s^2 = (1-\rho)P_T$ represents the transmit power of the IM waveform. Consequently, as ρ increases, the transmit power allocated for the IM waveform decreases, and that of the AN waveform increases.

The WPTx emits multitone IM waveforms where the available power is equally distributed among N_{a} active transmit antennas, whereas the generated AN is emitted from all antennas. Multitone signals with a bandwidth B are defined by the expression $(n-1)\Delta f_N$, where Δf_N represents the inter-carrier frequency spacing, set at 1 kHz and is employed in simulations The frequency of the first subband, f_1, is set at 100 kHz, while the subsequent subbands adhere to the frequency relationship $f_n = f_1 + \Delta f_N$. Note that WPT waveforms do not rely on CSI, although the CSI of the WPTx-IR link is available at the transmitter and is utilized in generating the AN. The simulation parameters regarding WPTx are provided in Table III.

We compare our simulation results with two benchmark schemes: MU-SWIPT [20] and Time Switching (TS)-SWIPT [46]. In both settings, $N_T = 6$ transmit antennas are assumed for TS-SWIPT and MU-SWIPT. In MU-SWIPT, matched filtering (MF) [36] is employed for the AP-IR and AP-ER links, each with a single receive antenna ($N_{\text{IR}} = 1$) at both the IR and EH. On the other hand, TS-SWIPT has $N_{\text{IR}} = 4$ for both the IR and EH, utilizing DC combining at the EH. In both settings, M-QAM is used for information signals, and real Gaussian (RG) signals are employed for energy signals. For the MU-SWIPT case, $a\%$ of the power is allocated to information transfer, while for the TS-SWIPT case, $b\%$ of the transmitted symbol frame is allocated to information transfer.

A. Energy harvesting capability

In this subsection, we investigated the benefits of the IM-based IH mechanism at the EH and present a comparative analysis that exhaustively evaluates energy harvesting capabilities for different N values and varying
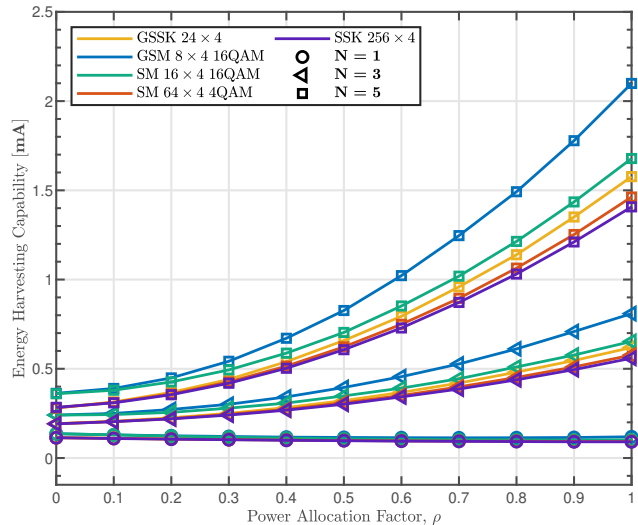

Fig. 3: The energy harvesting capability (z_{DC}) comparison of SM schemes with $\eta = 8$ for different N values with respect to varying power allocation factors, the EH is located at $d = 1.5$m from the WPTx.

ρ parameters. Figs. 3 and 4 illustrate that AN significantly affects the energy harvesting capability of the IH system since AN introduces interference on the EH end while facilitating secure WIT by disrupting Eve's signal. As the power allocation factor, ρ, increases, EH experiences more interference, which is advantageous for RF energy harvesting. Thus, higher ρ values contribute to improved energy harvesting capability across all IM schemes. As a result, the IH mechanism strategically enhances the system's energy harvesting capability while providing secure WIPT through the incorporation of AN.

It is noteworthy that all IM schemes exhibit nearly identical results in the case of CW signals ($N = 1$) for RF energy harvesting since the constant envelope characteristics of CW signals and also modulation schemes such as 4-QAM/PSK are not beneficial for energy harvesting with the utilized nonlinear rectifier model [34]. To illustrate the impact of higher-order modulation schemes on the rectifier's nonlinearity, Fig.3 compares SM schemes utilizing 4-QAM and 16-QAM. It is observed that 16-QAM outperforms 4-QAM in terms of energy harvesting capability due to higher M values inducing amplitude fluctuations, thereby improving the efficiency of RF-to-DC conversion within the rectifier [35]. Therefore, the modulation type impacts the system's energy harvesting capability [13].

Moreover, the comparison between Figs. 3 and 4 demonstrate that introducing multitone signals, coupled with IM schemes, enhances the energy harvesting capability across all IM schemes. As N increases, IM schemes exhibit distinct characteristics. The best performance results are acquired by
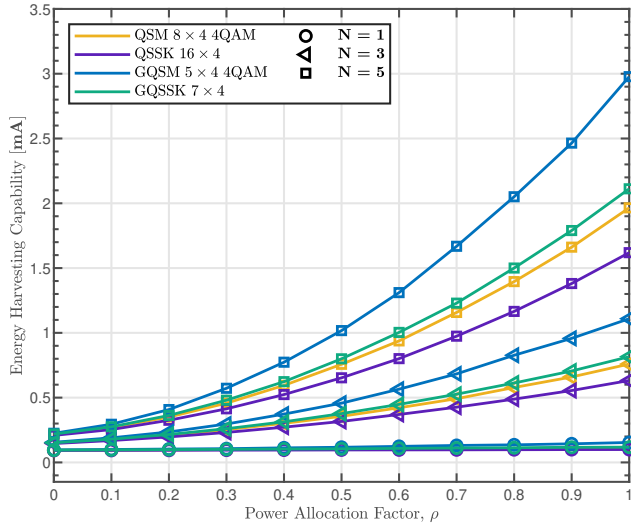
Fig. 4: The energy harvesting capability (z_{DC}) comparison of QSM schemes with $\eta = 8$ for different N values with respect to varying power allocation factors, the EH is located at $d = 1.5$m from the WPTx.

IM schemes that activate more than one antenna at a time and also select $\mathbf{w}_n$ values from the M-QAM constellations. Since IM schemes activate more antennas than those activating one antenna at a time to convey information, they achieve the same spectral efficiency with a reduced total number of antennas, such as GQSM and GSSK. Thus, dividing λ_u^2 among fewer antennas is profitable to leverage the strategic advantages of AN in terms of energy harvesting capability. Nonetheless, from the information harvesting perspective, increasing the total number of transmit antennas enhances the spectral efficiency of the IH system, allowing the transmission of more information.

Comparison with Benchmark Schemes: We compare the best and worst cases of the IH mechanism, namely GQSM and SSK, with benchmark schemes in Fig. 5 so as to highlight the advantages of the IH mechanism in terms of far-field WPT range. We assume that 70% of the power is allocated for energy harvesting in the MU-SWIPT case, and 70% of the transmitted
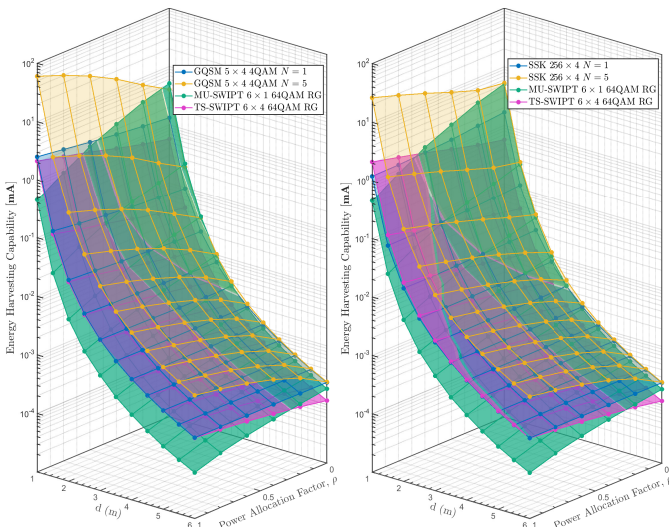
TABLE IV: RECEIVED POWER for IH and SWIPT.

WIPT Mechansim		Approx. d at received signal strength		
		-5 dBm	-10 dBm	-20 dBm
Information	$N = 1$	1.2m	1.4m	1.8m
Harvesting	$N = 5$	1.5m	1.8m	2.3m
MU-SWIPT	70%	1.0m	1.1m	1.5m
TS-SWIPT	70%	1.1m	1.2m	1.6m

frame is allocated for energy harvesting in the TS-SWIPT case. The IH system consistently outperforms the considered benchmark schemes, particularly in the scenario with $N = 5$, as the parameters d and ρ increase. Even when $N = 1$, the IH mechanism demonstrates its superiority against benchmark schemes, except in the case where ρ exceeds 0.6 for SSK. It is important to note that allocating 70% of the resources for RF energy harvesting is generally unfeasible for SWIPT systems, which prioritize allocating most resources to WIT rather than WPT, as presented in [44]. Despite this generous allocation, the IH system underscores its superiority in terms of range and energy harvesting capability. Notably, the IH mechanism adeptly leverages the benefits of AN, resulting in a secure and more efficient WPT mechanism through the use of IM techniques.

Furthermore, in the MU-SWIPT system, allocating P_T between information and energy signals is required, with both transmitted across all the transmit antennas. Additionally, deploying MF demands an equivalent number of RF chains to the number of transmit antennas, leading to increased power consumption at the transmitter. Meanwhile, the power consumption of the IH mechanism remains unaffected by the total number of antennas. Therefore, fewer RF chains are sufficient to capitalize on the benefits of IM schemes, contributing to a simpler and more power-efficient transmitter design [47].

In Table IV, we assess our system under average received signal strength constraints of $\{-5, -10, -20\}$ dBm to provide practical insights into the IH mechanism concerning rectenna sensitivity [48], [49]. The evaluation is based on identical setups depicted in Fig. 5(a) at $\rho = 0.4$. Our findings reveal that as N increases, the IH mechanism extends the range at the specified received signal strengths. Additionally, within these distances, the energy harvesting capability illustrated in Fig. 5(a) outperforms benchmarks, except in the case where the MU-SWIPT method outperforms the IH mechanism for $N = 1$.

B. Error performance

In this subsection, we investigate the BER performance of the proposed IM-based IH mechanism and present numerical results to support its merits. The BER of the IH mechanism for all IM schemes is plotted in Figs. 6 and 7 to illustrate the impact of multitone signals on information harvesting performance. Within the IH mechanism, N distinct subbands experience the same channel gains between the WPTx and IR, with AWGN added to those subbands per receive antenna. Consequently, the increase in N results in more noise in the received signal vector, detrimentally affecting the information-decoding process. Simulation results are validated with analytical results provided in (20) for the IR. As expected, the analytical curves
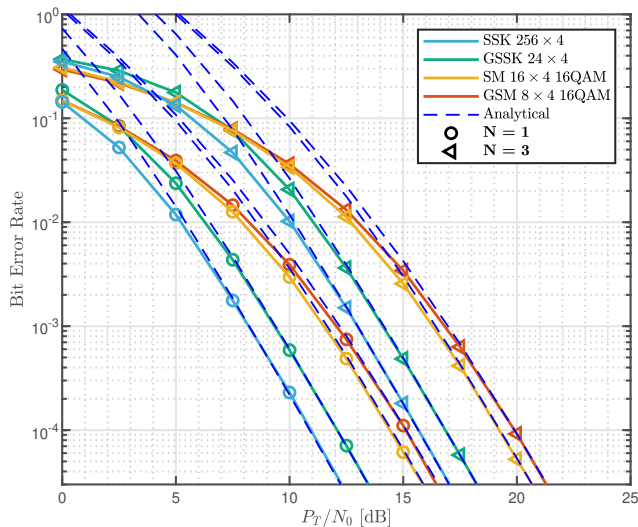

Fig. 5: Comparison of the energy harvesting capability (z_{DC}) for the IH mechanism (a) GQSM and (b) SSK with benchmark schemes across varying distances and power allocation factors.

Fig. 6: The ABER comparison at the IR for SM schemes with $\eta = 8$, $\rho = 0.2$ and for varying N parameters.
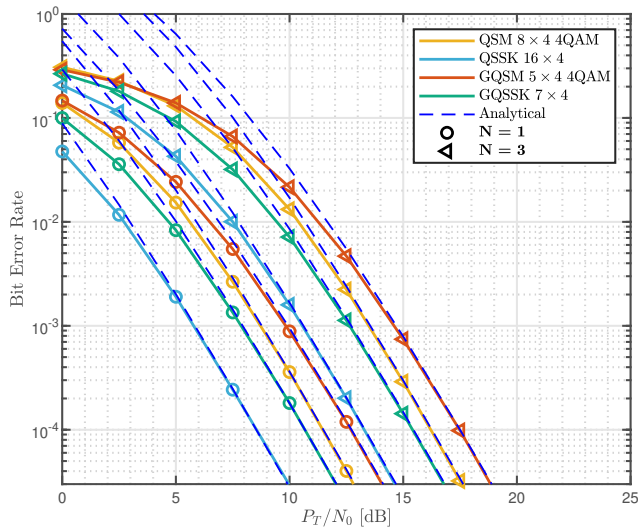

Fig. 7: The ABER comparison at the IR for QSM schemes with $\eta = 8$, $\rho = 0.2$ and for varying N parameters.

coincide with simulation results as P_T/N_0 increases. The BER of each IM scheme for single subband transmission is approximately 5 dB better than in the case where $N = 3$. Thus, there is a non-trivial tradeoff between the z_{DC} and the BER performance of the IH architecture. Figs. 6 and 7 also illustrate that best performance results are achieved when all bits are modulated in the spatial domain, particularly SSK and QSSK consistently exhibit superior results compared to the others. Thus, increasing the number of modulated bits in the spatial domain generally enhances the performance of IM schemes. Nonetheless, generalized variants of these techniques, such as GSSK, GQSM, and GQSSK, yield inferior outcomes due to the fact that generalized IM techniques introduce spatial correlation in the spatial domain, adversely affecting the IH system's performance in the end.

Comparison with Benchmark Schemes: In Fig. 8, we compare the BER performance of the IH mechanism, using SSK, QSSK, GSM, and GQSM techniques, against benchmark schemes that utilize 64-QAM and 256-QAM for WIT. For the MU-SWIPT
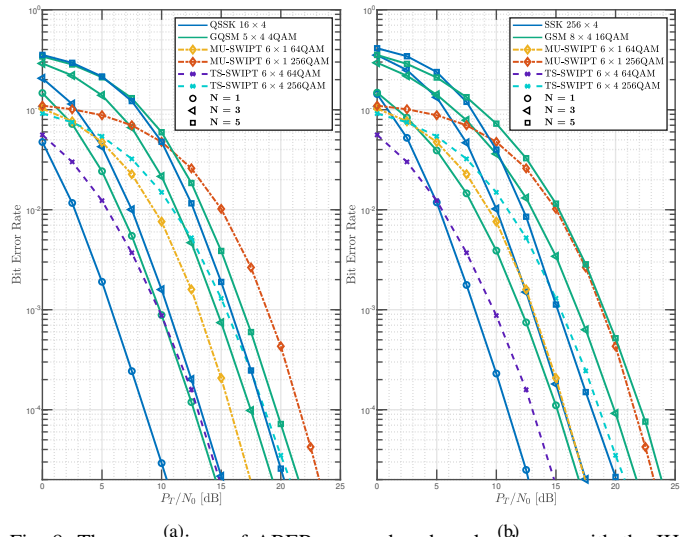

Fig. 8: The comparison of ABER among benchmark schemes with the IH mechanism: (a) QSSK and GQSM, and (b) SSK and GSM, where $\eta = 8$, $\rho = 0.2$, and varying N values.

and TS-SWIPT cases, 70% of the power and the transmitted frame are assigned for WIT, respectively. In the case of $N = 1$, the IH mechanism outperforms benchmarks across all IM schemes, except in the TS-SWIPT 64-QAM scenario against GSM. Noteworthy is the superior performance of QSSK over the MU-SWIPT 64-QAM case when $N = 3$. Remarkably, the spectral efficiency of the 64-QAM case for both benchmark schemes is only half that of the IM schemes. When the spectral efficiency of the benchmark schemes aligns with that of the IM schemes, the IH mechanism demonstrates superior BER results for $N = 3$ and $N = 5$ compared to the MU-SWIPT 256-QAM case. However, the results are almost identical for GSM, while the TS-SWIPT case outperforms GSM and GQSM when $N = 5$. Unlike the close BER performance of the IH mechanism to the TS-SWIPT case for $N = 3$ and $N = 5$, the IH mechanism reveals significant energy harvesting capability in the identical setup. Hence, the IH mechanism's superiority is attributed to its utilization of the antenna domain for conveying information, setting it apart from benchmark schemes. Consequently, the IH mechanism can establish a reliable communication channel with the contribution of IM schemes without disrupting the ongoing far-field WPT mechanism.

The impact of AN on Eve's BER performance is explored in Fig. 9, including the use of GSSK with $N_T = 7$, GSM with $N_T = 4$, and 4-QAM, QSSK with $N_T = 4$, as well as GQSSK with $N_T = 4$ schemes for $N = 1$, $N = 3$, and $N = 5$. Analytical curves become more precise as the P_T/N_0 increases. The simulation and analytical curves closely align in the high P_T/N_0 range, particularly when it exceeds 5 dB. Fig. 9 illustrates that the introduction of AN on larger subbands significantly disrupts Eve's ability to decode the transmitted data, resulting in a substantial deterioration in Eve's BER performance, which accounts for the protective effect of the IH mechanism against eavesdropping attempts.

C. Secrecy analysis

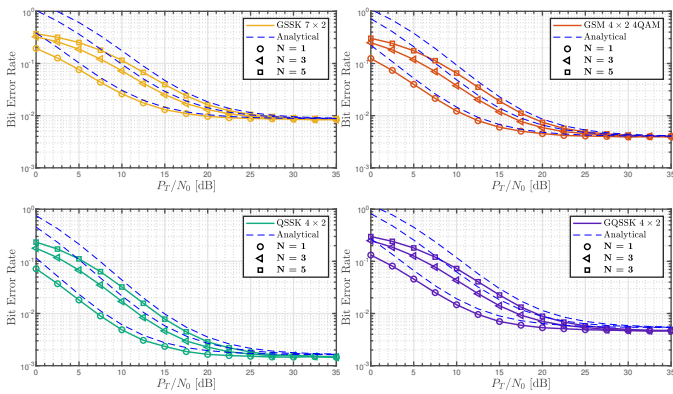Now, we investigate the ESR of the proposed IM-based IH schemes, including GSSK, QSSK, QSM, and GQSM, where

Fig. 9: The ABER comparison of Eve for (a) GSSK, (b) GSM, (c) QSSK, and (d) GQSSK with $\eta = 4$, $\rho = 0.025$, and varying values of the parameter N.

$N_T = 4$, $N_a = 2$, $N_{IR} = 2$, and 4-QAM is utilized when necessary, resulting in varying spectral efficiencies among the IM schemes with ρ set to 0.2 and 0.6, respectively. Figs. 10a and 10b reveal that for $\rho = 0.2$, the GSM scheme provides higher secrecy compared to the others, while for $\rho = 0.6$, QSSK outperforms all the schemes at low P_T/N_0 values with the expense of higher decoding complexity. In the high P_T/N_0 region, the GQSM scheme yields the best performance.

Comparison with Benchmark Schemes: In Figs. 10(a) and 10(b), ESR results are also compared with benchmark schemes, where $N_T = 4$, $N_{IR} = 1$ for MU-SWIPT, and $N_{IR} = 2$ for TS-SWIPT, both employing 16-QAM. In MU-SWIPT and TS-SWIPT cases, 70% of the power and the transmitted frame are allocated for WIT, respectively. In scenarios where $N = 3$ and $N = 5$, benchmark schemes initially exhibit better results compared to the IH mechanism at low P_T/N_0 values. However, as P_T/N_0 increases, ESR saturates for all cases, and the results become indistinguishable after reaching specific P_T/N_0 values except for the GQSM scheme, which persists in outperforming benchmarks. Moreover, allocating additional power to generate AN proves crucial in enhancing the secrecy performance of the IH mechanism, effectively preventing Eve from detecting injected data during information seeding. Additionally, the ESR performance of the IH mechanism is negatively influenced by an increasing number of subbands.

It is worth mentioning that the IH mechanism demands an ongoing WPT mechanism and $N_R > 1$ to achieve reliable WIT, as the information bits are injected into multitone waveforms through IM schemes. In contrast, the SWIPT systems can achieve WPT and WIT functions separately without relying on each other, and reliable communication can be achieved with $N_R = 1$ [15]. While opting for a higher number of subbands is advantageous for wireless power transmission, it is essential to carefully consider the cumulative impact of channel effects and Gaussian noise on the receiver side since these factors could degrade overall system performance, particularly in terms of WIT. Furthermore, an increased N value of multitone signals induces high PAPR characteristics, which result in unwanted amplitude distortion in the transmit signal [50] such that a proper transmitter design for the IH mechanism is needed while it is likely to design a SWIPT system which is not based on multitone signals.
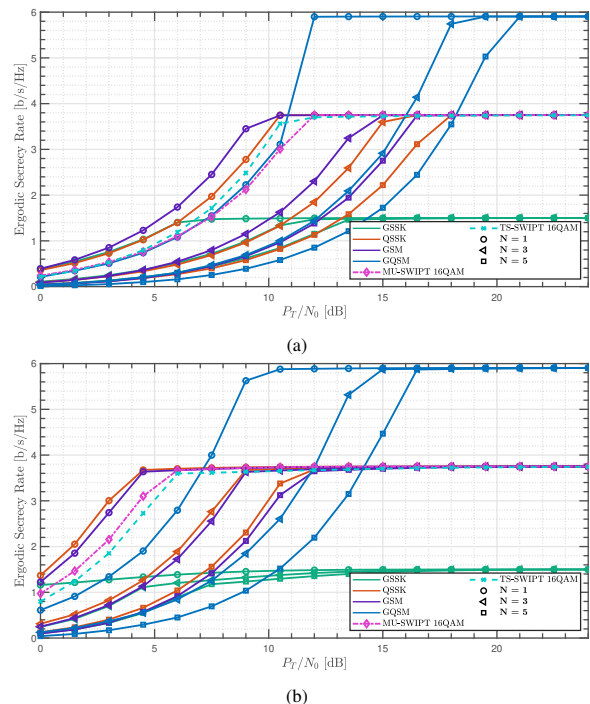

Fig. 10: The ESR comparison of the IH mechanism with benchmark schemes (30) (a) $\rho = 0.2$ and (b) $\rho = 0.6$, with varying N values.

VI. CONCLUDING REMARKS

The massive connections of simple nodes present significant challenges to the communication infrastructure as we move towards 6G technology. Establishing sustainable, green, and secure communication accounts for providing synergistic ways of delivering information and power to IoT devices. This paper presents a comprehensive framework for the IH mechanism, leveraging existing far-field WPT mechanisms to enable wireless communication through exploiting diverse IM techniques. The presented simulations and analytical derivations underline the advantages of IM-based IH mechanisms, particularly in terms of energy harvesting capabilities at the EH and the reliability and secrecy of the communication at the IR. In this respect, the results reveal that the IH mechanism can extend the far-field WPT range and energy harvesting capability while ensuring secure and reliable WIT through efficient transmitter design by harnessing the amalgamation of multitone signals with IM techniques. In summary, the IH mechanism holds significant potential for IoT devices in the 6G era by introducing a novel communication channel atop existing WPT mechanisms.

ACKNOWLEDGMENT

REFERENCES

[1] Y. Zhang and B. Long, "A review of 5G-advanced service and system aspects standardization in 3GPP," in *2022 IEEE/CIC Int. Conf. Commun. in China (ICCC Workshops)*, 2022, pp. 94–99.

[2] S. Naser, L. Bariah, S. Muhaidat, and E. Basar, "Zero-energy devices empowered 6G networks: Opportunities, key technologies, and challenges," 2023. [Online]. Available: https://www.techrxiv. org/articles/preprint/Zero-Energy_Devices_Empowered_6G_Networks_ Opportunities_Key_Technologies_and_Challenges/21558030

[3] Y. Liu, D. Li, H. Dai, C. Li, and R. Zhang, "Understanding the impact of environmental conditions on zero-power Internet of Things: An experimental evaluation," *IEEE Wireless Commun.*, pp. 1–8, 2022.

[4] N. Tesla, "The transmission of electrical energy without wires," *Electrical World and Engineer*, vol. 1, pp. 21–24, 1904.

[5] C. R. Valenta and G. D. Durgin, "Harvesting wireless power: Survey of energy-harvester conversion efficiency in far-field, wireless power transfer systems," *IEEE Microw. Mag.*, vol. 15, no. 4, pp. 108–120, 2014.

[6] X. Gu, P. Burasa, S. Hemour, and K. Wu, "Recycling ambient RF energy: Far-field wireless power transfer and harmonic backscattering," *IEEE Microw. Mag.*, vol. 22, no. 9, pp. 60–78, 2021.

[7] G. Pan, P. D. Diamantoulakis, Z. Ma, Z. Ding, and G. K. Karagiannidis, "Simultaneous lightwave information and power transfer: Policies, techniques, and future directions," *IEEE Access*, vol. 7, pp. 28 250–28 257, 2019.

[8] B. Clerckx, A. Costanzo, A. Georgiadis, and N. Borges Carvalho, "Toward 1G mobile power networks: RF, signal, and system designs to make smart objects autonomous," *IEEE Microw. Mag.*, vol. 19, no. 6, pp. 69–82, 2018.

[9] M.-L. Ku, W. Li, Y. Chen, and K. J. Ray Liu, "Advances in energy harvesting communications: Past, present, and future challenges," *IEEE Commun. Surv. Tutor.*, vol. 18, no. 2, pp. 1384–1412, 2016.

[10] D. V. Leemput, A. Sabovic, K. Hammoud, J. Famaey, S. Pollin, and E. D. Poorter, "Energy harvesting for wireless IoT use cases: A generic feasibility model and tradeoff study," *IEEE Internet Things J.*, pp. 1–1, 2023.

[11] A. Costanzo and D. Masotti, "Smart solutions in smart spaces: Getting the most from far-field wireless power transfer," *IEEE Microw. Mag.*, vol. 17, no. 5, pp. 30–45, 2016.

[12] S. Shen and B. Clerckx, "Joint waveform and beamforming optimization for MIMO wireless power transfer," *IEEE Trans. Commun.*, vol. 69, no. 8, pp. 5441–5455, 2021.

[13] M. Cansiz, D. Altinel, and G. K. Kurt, "Effects of different modulation techniques on charging time in RF energy-harvesting system," *IEEE Trans. Instrum. Meas.*, vol. 69, no. 9, pp. 6904–6911, 2020.

[14] S. Bi, Y. Zeng, and R. Zhang, "Wireless powered communication networks: an overview," *IEEE Wireless Commun.*, vol. 23, no. 2, pp. 10–18, 2016.

[15] T. D. Ponnimbaduge Perera, D. N. K. Jayakody, S. K. Sharma, S. Chatzinotas, and J. Li, "Simultaneous wireless information and power transfer (SWIPT): Recent advances and future challenges," *IEEE Commun. Surveys Tuts.*, vol. 20, no. 1, pp. 264–302, 2018.

[16] M. Uysal, S. Ghasvarianjahromi, M. Karbalayghareh, P. D. Diamantoulakis, G. K. Karagiannidis, and S. M. Sait, "SLIPT for underwater visible light communications: Performance analysis and optimization," *IEEE Trans. Wireless Commun.*, vol. 20, no. 10, pp. 6715–6728, 2021.

[17] W. Liu, X. Zhou, S. Durrani, and P. Popovski, "SWIPT with practical modulation and RF energy harvesting sensitivity," in *Proc. IEEE Int. Conf. Commun. (ICC)*, 2016, pp. 1–7.

[18] G. Amarasuriya, E. G. Larsson, and H. V. Poor, "Wireless information and power transfer in multiway massive MIMO relay networks," *IEEE Trans. Wireless Commun.*, vol. 15, no. 6, pp. 3837–3855, 2016.

[19] G. Paolini, A. Quddious, D. Chatzichristodoulou, D. Masotti, S. Nikolaou, and A. Costanzo, "An energy-autonomous SWIPT RFID tag for communication in the 2.4 GHz ISM band," in *3rd URSI Atlantic and Asia Pacific Radio Science Meeting (AT-AP-RASC)*, 2022, pp. 1–4.

[20] J. Xu, L. Liu, and R. Zhang, "Multiuser MISO beamforming for simultaneous wireless information and power transfer," *IEEE Trans. Signal Process.*, vol. 62, no. 18, pp. 4798–4810, 2014.

[21] S. N. K. Veedu, M. Mozaffari, A. Höglund, E. A. Yavuz, T. Tirronen, J. Bergman, and Y.-P. E. Wang, "Toward smaller and lower-cost 5G devices with longer battery life: An overview of 3GPP release 17 RedCap," *IEEE Commun. Stand. Mag.*, vol. 6, no. 3, pp. 84–90, 2022.

[22] D. Xu and H. Zhu, "Secure transmission for SWIPT IoT systems with full-duplex IoT devices," *IEEE Internet Things J.*, vol. 6, no. 6, pp. 10 915–10 933, 2019.

[23] Y. Huang, M. Liu, and Y. Liu, "Energy-efficient SWIPT in IoT distributed antenna systems," *IEEE Internet Things J.*, vol. 5, no. 4, pp. 2646–2656, 2018.

[24] I. Krikidis and C. Psomas, "Tone-index multisine modulation for SWIPT," *IEEE Signal Process. Lett.*, vol. 26, no. 8, pp. 1252–1256, 2019.

[25] Y. Nakamoto, N. Hasegawa, T. Hirakawa, and Y. Ohta, "A study on OFDM modulation suitable for wireless power transfer," in *Wireless Power Week (WPW)*, 2022, pp. 21–24.

[26] M. C. Ilter, R. Wichman, M. Säily, and J. Hämäläinen, "Information harvesting for far-field wireless power transfer," *IEEE Internet Things Mag.*, vol. 5, no. 2, pp. 127–132, 2022.

[27] N. Wang, P. Wang, A. Alipour-Fanid, L. Jiao, and K. Zeng, "Physical-layer security of 5G wireless networks for IoT: Challenges and opportunities," *IEEE Internet Things J.*, vol. 6, no. 5, pp. 8169–8181, 2019.

[28] S. Goel and R. Negi, "Guaranteeing secrecy using artificial noise," *IEEE Trans. Wireless Commun.*, vol. 7, no. 6, pp. 2180–2189, 2008.

[29] L. Lv, Z. Ding, Q. Ni, and J. Chen, "Secure MISO-NOMA transmission with artificial noise," *IEEE Trans. Veh. Technol.*, vol. 67, no. 7, pp. 6700–6705, 2018.

[30] Y. Gu, Z. Wu, Z. Yin, and X. Zhang, "The secrecy capacity optimization artificial noise: A new type of artificial noise for secure communication in MIMO system," *IEEE Access*, vol. 7, pp. 58 353–58 360, 2019.

[31] M. C. Ilter, E. Basar, R. Wichman, and J. Hämäläinen, "Information harvesting for far-field RF power transfer through index modulation," in *Proc. IEEE Glob. Commun. Conf. (GLOBECOM)*, 2022.

[32] M. C. Ilter, R. Wichman, J. Hämäläinen, and S. Ikki, "A new information harvesting mechanism for far-field wireless power transfer," in *Proc. IEEE Veh. Tech. Conf. (VTC-Spring)*, 2023, pp. 1–6.

[33] P. N. Alevizos and A. Bletsas, "Sensitive and nonlinear far-field RF energy harvesting in wireless communications," *IEEE Trans. Wireless Commun.*, vol. 17, no. 6, pp. 3670–3685, 2018.

[34] B. Clerckx, J. Kim, K. W. Choi, and D. I. Kim, "Foundations of wireless information and power transfer: Theory, prototypes, and experiments," *Proc. IEEE Proc.*, vol. 110, no. 1, pp. 8–30, 2022.

[35] B. Clerckx and E. Bayguzina, "Waveform design for wireless power transfer," *IEEE Trans. Signal Process.*, vol. 64, no. 23, pp. 6313–6328, 2016.

[36] J. Kim, B. Clerckx, and P. D. Mitcheson, "Signal and system design for wireless power transfer: Prototype, experiment and validation," *IEEE Trans. Wireless Commun.*, vol. 19, no. 11, pp. 7453–7469, 2020.

[37] J. Jeganathan, A. Ghrayeb, and L. Szczecinski, "Generalized space shift keying modulation for MIMO channels," in *Proc. IEEE Int. Symp. on Pers., Indoor and Mobile Radio Commun. (PIMRC)*, 2008, pp. 1–5.

[38] R. Mesleh, S. S. Ikki, and H. M. Aggoune, "Quadrature spatial modulation," *IEEE Trans. Veh. Technol.*, vol. 64, no. 6, pp. 2738–2742, 2015.

[39] B. Clerckx, R. Zhang, R. Schober, D. W. K. Ng, D. I. Kim, and H. V. Poor, "Fundamentals of wireless information and power transfer: From RF energy harvester models to signal and system designs," *IEEE J. Sel. Areas Commun.*, vol. 37, no. 1, pp. 4–33, 2019.

[40] M. Di Renzo and H. Haas, "A general framework for performance analysis of space shift keying (SSK) modulation for MISO correlated Nakagami-m fading channels," *IEEE Trans. Commun.*, vol. 58, no. 9, pp. 2590–2603, 2010.

[41] Z. Huang, Z. Gao, and L. Sun, "Anti-eavesdropping scheme based on quadrature spatial modulation," *IEEE Commun. Lett.*, vol. 21, no. 3, pp. 532–535, 2017.

[42] Y. Wei, L. Wang, and T. Svensson, "Analysis of secrecy rate against eavesdroppers in MIMO modulation systems," in *Int. Conf. on Wireless Commun. Signal Process. (WCSP)*, 2015, pp. 1–5.

[43] U. Singh, M. R. Bhatnagar, and T. A. Tsiftsis, "Secrecy analysis of SSK modulation: Adaptive antenna mapping and performance results," *IEEE Trans. Wireless Commun.*, vol. 20, no. 7, pp. 4614–4630, 2021.

[44] X. Zhou, R. Zhang, and C. K. Ho, "Wireless information and power transfer: Architecture design and rate-energy tradeoff," *IEEE Trans. Commun.*, vol. 61, no. 11, pp. 4754–4767, 2013.

[45] Federal Commun. Comm., "47 CFR Part15-Radio Frequency Devices," Washington, DC, USA, 2016.

[46] S. Kang, H. Lee, S. Hwang, and I. Lee, "Time switching protocol for multi-antenna SWIPT systems," *IEEE Wireless Commun. and Netw. Conf. (WCNC)*, pp. 1–6, 2020.

[47] E. Basar, M. Wen, R. Mesleh, M. Di Renzo, Y. Xiao, and H. Haas, "Index modulation techniques for next-generation wireless networks," *IEEE Access*, vol. 5, pp. 16 693–16 746, 2017.

[48] J. Kim, B. Clerckx, and P. D. Mitcheson, "Experimental analysis of harvested energy and throughput trade-off in a realistic SWIPT system," in *IEEE Wireless Power Transfer Conf. (WPTC)*, 2019, pp. 1–5.

[49] N. Ayir and T. Riihonen, "Efficiency–throughput trade-off of pulsed rf waveforms in simultaneous wireless information and power transfer," in *IEEE Wireless Power Technol. Conf. Expo (WPTCE)*, 2023, pp. 1–5.

[50] J. J. Park, J. H. Moon, H. H. Jang, and D. I. Kim, "Performance analysis of power amplifier nonlinearity on multi-tone SWIPT," *IEEE Wireless Commun. Lett.*, vol. 10, no. 4, pp. 765–769, 2021.